

THE 2L1S/1L2S DEGENERACY FOR TWO MICROLENSING PLANET CANDIDATES DISCOVERED BY THE KMTNET SURVEY IN 2017

I.-G. SHIN^{H1,K1}, J. C. YEE^{H1}, A. GOULD^{K1,E1,E2}, M. D. ALBROW^{K3}, S.-J. CHUNG^{K1,K2}, C. HAN^{K5}, K.-H. HWANG^{K1}, Y. K. JUNG^{K1}, Y.-H. RYU^{K1}, Y. SHVARTZVALD^{E3}, W. ZANG^{E4}, M. T. PENNY^{E1}, P. FOUQUÉ^{E5,E6}, C.-U. LEE^{K1,K2}, S.-M. CHA^{K1,K4}, D.-J. KIM^{K1}, H.-W. KIM^{K1,K2}, S.-L. KIM^{K1,K2}, Y. LEE^{K1,K4}, D.-J. LEE^{K1}, B.-G. PARK^{K1,K2}, R. W. POGGE^{E1}

^{H1}Harvard-Smithsonian Center for Astrophysics, 60 Garden St., Cambridge, MA 02138, USA

^{K1}Korea Astronomy and Space Science Institute, 776 Daedeokdae-ro, Yuseong-Gu, Daejeon 34055, Republic of Korea

^{K2}Korea University of Science and Technology, 217 Gajeong-ro, Yuseong-gu, Daejeon 34113, Republic of Korea

^{K3}University of Canterbury, Department of Physics and Astronomy, Private Bag 4800, Christchurch 8020, New Zealand

^{K4}School of Space Research, Kyung Hee University, Giheung-gu, Yongin, Gyeonggi-do, 17104, Republic of Korea

^{K5}Department of Physics, Chungbuk National University, Cheongju 28644, Republic of Korea

^{E1}Department of Astronomy, Ohio State University, 140 W. 18th Ave., Columbus, OH 43210, USA

^{E2}Max-Planck-Institute for Astronomy, Königstuhl 17, 69117 Heidelberg, Germany

^{E3}IPAC, Mail Code 100-22, Caltech, 1200 E. California Blvd., Pasadena, CA 91125, USA

^{E4}Physics Department and Tsinghua Centre for Astrophysics, Tsinghua University, Beijing 100084, People's Republic of China

^{E5}CFHT Corporation, 65-1238 Mamalahoa Hwy, Kamuela, Hawaii 96743, USA

^{E6}Université de Toulouse, UPS-OMP, IRAP, Toulouse, France

Draft version March 1, 2019

ABSTRACT

We report two microlensing planet candidates discovered by the KMTNet survey in 2017. However, both events have the 2L1S/1L2S degeneracy, which is an obstacle to claiming the discovery of the planets with certainty unless the degeneracy can be resolved. For KMT-2017-BLG-0962, the degeneracy cannot be resolved. If the 2L1S solution is correct, KMT-2017-BLG-0962 might be produced by a super Jupiter-mass planet orbiting a mid-M dwarf host star. By contrast, for KMT-2017-BLG-1119, high-resolution observations of the baseline object strongly support the 1L2S interpretation rather than the planetary interpretation. This study shows the problem of resolving 2L1S/1L2S degeneracy exists over a much wider range of conditions than those considered by the theoretical study of Gaudi (1998).

Subject headings: gravitational lensing: micro – exoplanets

1. INTRODUCTION

The basic requirements for the statistical studies of planets are detections of planets and the determination of planet properties. However, discoveries and characterizations of microlensing planets depend on the interpretation of anomalies in the observed light curves. Even when these anomalies can be described by a planetary model, there may exist alternative interpretations that also provide sufficient descriptions for the putative planetary anomalies. In other words, degenerate solutions of the light curves can be obstacles to prevent either secure discoveries of planets or the unique determination of their properties.

For example, the degeneracy between two interpretations of the binary-lens and single-source (2L1S) and the single-lens and binary-source (1L2S) can be a severe obstacle. If this 2L1S/1L2S degeneracy exists, we cannot claim a secure discovery of the planet unless the degeneracy is resolved. Gaudi (1998) first pointed out this 2L1S/1L2S degeneracy by showing that a certain class of 1L2S model can resemble a planetary anomaly in the lensing light curve. In particular, he focused on planetary events that exhibit small, short-duration positive deviations from a single-lens, single-source (1L1S) light curve. To produce a similar anomaly on the light curve using a 1L2S model, the brightness of the companion should be much fainter than the primary. In addition, the companion should pass very close (in projection) to the lens.

Indeed, there are discoveries of microlensing planet candidates, which could be interpreted by both 2L1S and 1L2S models. Beaulieu et al. (2006) found a clear planetary devia-

tion (i.e., a small, short-duration positive deviation) in a microlensing event, OGLE-2005-BLG-390. They also found the 2L1S/1L2S degeneracy that plausibly described the anomaly. However, the 1L2S interpretation was rejected by the detailed light curve analysis. Thus, they could claim the secure discovery of a planet, whose mass they estimated to be $5.5 M_{\oplus}$. Hwang et al. (2013) also showed a microlensing event that had the 2L1S/1L2S degeneracy. The light curve of this work exhibits a planet-like anomaly (i.e., the strong positive deviation) that can be explained by either the 2L1S (including a planet) or 1L2S interpretations. They successfully resolved this degeneracy using multi-band observations revealing that the event was produced by two sources, rather than a planetary system. In addition, Dominik et al. (2019) recently presented a long timescale ($t_E \sim 300$ days) microlensing event, which can be explained either 2L1S or 1L2S interpretations. Their 2L1S model indicates that the lens system might be a planet with the mass $\sim 45 M_{\oplus}$ orbiting an M-dwarf host star ($\sim 0.35 M_{\odot}$). However, they also find a competitive 1L2S model that indicates that the lens might be a brown-dwarf ($0.046 M_{\odot}$). The light curve data cannot resolve this degeneracy, but they suggest future observations may be able to resolve this severe degeneracy.

However, in practice, we have found that the 2L1S/1L2S degeneracy can be extended to cases beyond the extreme flux case considered by Gaudi (1998), e.g., Jung et al. (2017a), Dominik et al. (2019), and events in this work. In Jung et al. (2017a), the light curve of the event showed a broad asymmetry with small additional deviations in the wing. This anomaly can be adequately described by both the 2L1S (i.e., a plane-

tary lens system) and the 1L2S interpretations. This event was produced by close to equal-luminous binary sources in contrast to the case of Gaudi (1998). They resolved this degeneracy using detailed modeling of the densely covered light curve. In Dominik et al. (2019), they showed that the planet-like anomaly in the 2L1S case could be produced when the source passes close to the central caustic, i.e., a high-magnification event. This anomaly is different from Gaudi's case, which is produced when the source approaches one of planetary caustics. They noted that the 1L2S model with a small flux ratio of binary sources can produce this planet-like anomaly in contrast to Gaudi's case.

In addition, microlensing events showing more complex anomalies have been found. These events can be described by more complicated multiple-lens and multiple-source interpretations. For example, Jung et al. (2017b) showed a degeneracy caused by 3L1S and 2L2S interpretations. Moreover, Hwang et al. (2018) showed an extreme case (i.e., exomoon candidate) of a three-fold degeneracy with 3L1S, 2L2S, and 1L3S interpretations. In particular, the degeneracy becomes severe when the observations do not optimally cover the anomalies in the light curves.

Here we analyze two microlensing events, KMT-2017-BLG-0962 and KMT-2017-BLG-1119, that were discovered in 2017 by the Korea Microlensing Telescope Network (KMTNet; Kim et al. 2016) alone. We reveal that these events are planet candidates by analyzing the light curves using the 2L1S interpretation. For KMT-2017-BLG-0962, the mass ratio ($q = M_{\text{planet}}/M_{\text{host}}$) is ~ 0.01 , which indicates that the companion in the lens system might be a Jupiter-class planet under the assumption of an M-dwarf host star. For KMT-2017-BLG-1119, the mass ratio is ~ 0.06 , which is relatively large to be regarded as a planetary companion. However, the Einstein timescale (t_E) of this event is very short, i.e., $t_E \sim 3.5$ days. This short timescale implies that the event can be produced by a planetary lens system¹. However, both light curves can also be well described using the 1L2S interpretation.

We present KMTNet observations of these planet candidates in Section 2. In Section 3, we present analyses of the light curves and the degeneracies. Then, we discuss the possibilities of resolving the degeneracies in Section 4. In Section 5, we present the possible properties of planet candidates determined using the Bayesian analyses. Lastly, in Section 6, we present our conclusion with the difference between a Gaudi (1998)-type degeneracy and this work. Additionally, we provide details of the 1L2S interpretations for the modeling in Appendix A.

2. KMTNET OBSERVATIONS

KMTNet is a second-generation microlensing survey consisting of a telescope network composed of three identical 1.6 m telescopes located at three sites in the southern hemisphere: the Cerro Tololo Inter-American Observatory in Chile (KMTC), the South African Astronomical Observatory in South Africa (KMTS), and the Siding Spring Observatory in Australia (KMTA). These well-separated time zones can provide near-continuous observations, weather permitting. In addition, the cameras of the KMTNet survey have a wide field

¹ The Einstein timescale is a crossing time that the source transverses the Einstein ring radius (θ_E), i.e., $t_E \propto \theta_E$. The size of θ_E is directly related to the mass of the lens system (M), i.e., $\theta_E \propto \sqrt{M/D_{\text{rel}}}$ where $D_{\text{rel}} \equiv (D_L^{-1} - D_S^{-1})^{-1}$. D_L and D_S are distances to the lens and source, respectively. Thus, $t_E \propto \sqrt{M}$, which are of order a month for typical microlensing events.

of view (FOV: 4 deg^2). These wide FOV yield high-cadence observations that are optimized to capture planetary anomalies caused by various types of planets. Thus, in general, the KMTNet survey (i.e., a second-generation microlensing survey) is less dependent on follow-up observations.

KMTNet alone discovered the two planet candidates presented in this work. The events were found by the KMTNet Event Finder algorithm (Kim et al. 2018), which was run after the end of the 2017 microlensing season. No real-time alert was issued for these events, either by KMTNet or other microlensing groups. Hence, no useful real-time photometric follow-up observations were taken².

2.1. KMT-2017-BLG-0962

KMT-2017-BLG-0962 occurred on source(s) located at $(\alpha, \delta)_{\text{J2000}} = (17^h 46^m 48^s.54, -26^\circ 10' 48''.07)$ corresponding to the Galactic coordinates $(l, b) = (2.^{\circ}49, 1.^{\circ}21)$. This event is located in the KMT-field, BLG18 (see Figure 12 of Kim et al. 2018), which has the nominal observational cadence 1hr^{-1} . During the event, the cadence was 1hr^{-1} at KMTC. For the other observations, the cadence was 0.75hr^{-1} . In Figure 1, we present KMTNet observations of this event with a 1L1S model curve as a reference to clearly show the anomaly in the light curve. There exist clear perturbations around the peak of the event, $\text{HJD}' (= \text{HJD} - 2450000) \sim 7871.5$.

2.2. KMT-2017-BLG-1119

KMT-2017-BLG-1119 occurred on source(s) located at $(\alpha, \delta)_{\text{J2000}} = (17^h 52^m 10^s.63, -33^\circ 01' 05''.30)$ corresponding to the Galactic coordinates $(l, b) = (-2.^{\circ}78, -3.^{\circ}30)$. This event is located in the KMT-field, BLG22, which also has the nominal cadence 1hr^{-1} . During the event, this was an actual cadence for KMTC observations. For KMTS and KMTA observations, the cadence was switched from 1hr^{-1} to 0.75hr^{-1} at $\text{HJD}' \sim 7971.25$, i.e., just after the event peaked. In Figure 2, we present the KMTNet observations of this event. The observations show deviations ($\text{HJD}' \sim 7968.5$ and ~ 7971.0) from the 1L1S model.

3. DEGENERATE MODELS

Because both events show clear anomalies in the observed light curves, we analyze the light curves using both 2L1S and 1L2S interpretations. For each interpretation, we build model light curves using an appropriate parameterization. Then we minimize the χ^2 difference between the model and observations by using a Markov Chain Monte Carlo (MCMC) algorithm (Dunkley et al. 2005).

During the modeling process, the uncertainties of observations are rescaled using the equation, $e_{\text{new}} = \kappa_{\text{obs}} e_{\text{old}}$, where the e_{new} and e_{old} are rescaled and original uncertainties, respectively. The coefficient κ_{obs} , an error rescaling factor for each data set, is defined based on the best-fit model having the lowest χ^2 value. By making sure each data

² KMT-2017-BLG-1119 was in fact serendipitously observed by the *Spitzer* satellite because it lies within the IRAC camera field of view of another event (OGLE-2017-BLG-0019) that was chosen for observations (see Yee et al. 2015). Unfortunately, these observations ended (due to sun-angle restrictions) on $\text{JD} - 2450000.0 \sim 7967.0$, just two days before the peak of this very short event. In principle, if the lens were traveling approximately east, the source could nevertheless have been significantly magnified. However, we have checked the images and found that the *Spitzer* light curve of KMT-2017-BLG-1119 is essentially flat. Thus, no meaningful constraints can be placed on this system from the *Spitzer* data.

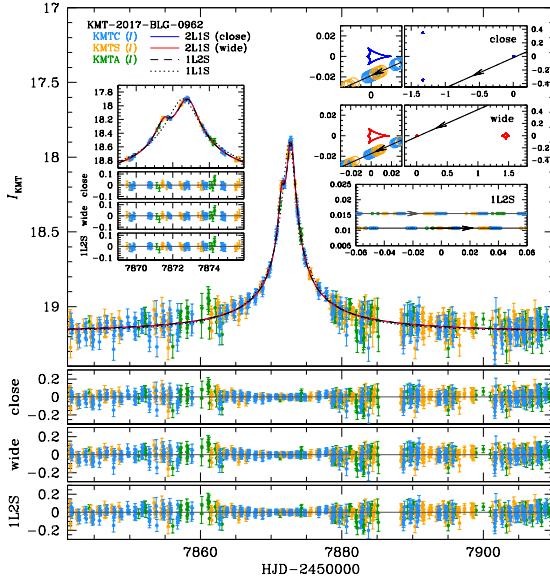


FIG. 1.— Degenerate models of KMT-2017-BLG-0962. The solid lines in red and blue indicate the 2L1S model light curves of the close and wide cases, respectively. The dashed line in black indicates the 1L2S model light curve. The dotted line indicates the 1L1S model light curve for this event. Left-side inner panels show a zoom-in for the anomaly part of the light curve with residuals. Right-side inner panels present geometries of 2L1S (upper and middle panels for the close and wide cases) and 1L2S (bottom panel) models. Three bottom panels show residuals between each model and observations.

point contributes on average $\Delta\chi^2 \sim 1$, we can quantitatively compare the degenerate models. For KMT-2017-BLG-0962 and KMT-2017-BLG-1119, the sets of error rescaling factors are $(\kappa_{\text{KMTC}}, \kappa_{\text{KMTS}}, \kappa_{\text{KMTA}}) = (1.244, 1.239, 1.392)$ and $(1.211, 1.120, 1.192)$, respectively.

3.1. Parameterization of the 2L1S Interpretation

To build a standard 2L1S model light curve, seven basic parameters are required to describe the caustic form and the source trajectory. Two parameters (s and q) determine the caustic form. The value s represents the projected separation between the lenses in units of the angular Einstein ring radius (θ_E). Conventionally, cases of $s < 1$ and $s > 1$ are referred to “close” and “wide”, respectively. The mass ratio of the lenses is defined as $q = M_2/M_1$ where M_1 and M_2 are masses of first and second bodies, respectively. These close and wide cases can yield a close/wide degeneracy caused by similarities in the magnification pattern, which are induced by an intrinsic symmetry in the lens equation (Griest & Safizadeh 1998; Dominik 1999).

Four parameters (t_0 , u_0 , t_E , and α) describe the source trajectory: t_0 is the time when the source most closely approaches to the reference position of the lens system (this reference position is centered at the positions of $s[1-(1+q)^{-1}]$ and $s^{-1}q/(1+q)$ for the close ($s < 1$) and wide ($s > 1$) cases, respectively), u_0 is the separation at the time of t_0 , t_E is the Einstein timescale defined as the time for the source to cross the Einstein ring radius of the event, and α is the angle of the source trajectory with respect to the binary axis of the lens system. The geometry of a microlensing event produced by 2L1S is built using these six parameters, which determine the magnification as a function of time, i.e., the microlensing light curve. The finite angular size of the source moderates the magnification. To account for the finite source effect, the final parameter, ρ_* , is required, which is defined as the angular source radius (θ_*) scaled by θ_E . In addition, we introduce two

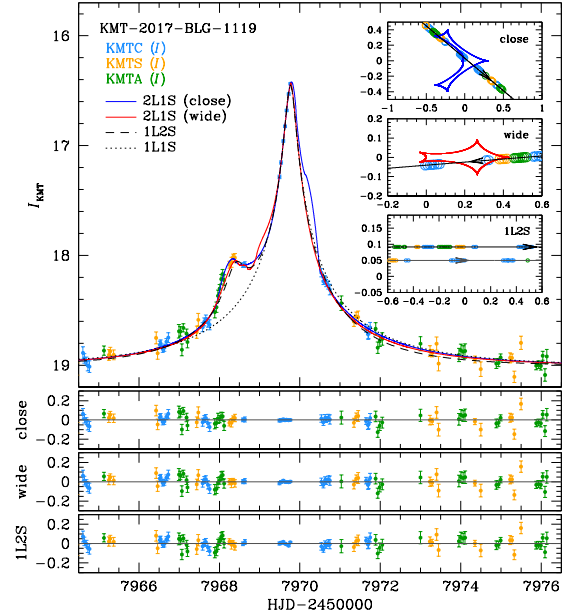


FIG. 2.— Degenerate models of KMT-2017-BLG-1119. The description is the same as for Figure 1.

additional parameters, $F_{\text{S,obs}}$ (source flux) and $F_{\text{B,obs}}$ (blending flux), for each data set, which are used to scale the model to the data. These parameters are determined based on the model using the least-square fitting method.

3.2. Parameterization of the 1L2S Interpretation

A standard 1L2S model light curve is built using a superposition of two 1L1S light curves induced by each source. The trajectory of each source yields the individual magnification of its 1L1S light curve. For the 1L2S model light curve, the final magnification is calculated by superposing magnifications of both sources weighted by the flux ratio of source stars. To describe the source trajectories, there are two parameterizations. The first parameterization (hereafter, A-type) describes the trajectory of each source, individually. In contrast, the second parameterization (hereafter, B-type) describes the barycenter motion of the binary-source system. Then, from the position of the barycenter, the position of each source is derived. In Appendix A, we provide detailed descriptions of these parameterizations and discuss the pros and cons of the two types. In this work, because the merits of the two types are different, we adopt the A-type for the basic 1L2S modeling (Section 3.3 and 3.4). For testing the higher-order effects, we adopt the B-type (Section 3.5).

3.3. Degeneracy in KMT-2017-BLG-0962

For KMT-2017-BLG-0962, we find that the observed light curve can be described using either 2L1S and 1L2S interpretations. In Figure 1, we present the observed data and model light curves of this event with geometries of the 2L1S and 1L2S interpretations. We also present residuals between the models and observations. In Table 1, we present the model parameters of best-fit models with χ^2 between the models and observations. The 2L1S model indicates that this event can be caused by a planetary lens system with a mass ratio $q \sim 0.01$ between the lens components. However, there is a degeneracy between the close and wide solutions. At the same time, the 1L2S model implies that the event can also be caused by a binary-source system. The planetary model (2L1S models

TABLE 1
BEST-FIT PARAMETERS OF DEGENERATE MODELS

KMT-2017-BLG-0962	2L1S (close)	2L1S (wide)	IL2S	
χ^2/N_{data}	1918.423/1918	1918.687/1918	χ^2/N_{data}	1919.026/1918
t_0 (HJD')	$7872.514^{+0.009}_{-0.003}$	$7872.536^{+0.011}_{-0.015}$	$t_{0,S1}$	$7871.478^{+0.024}_{-0.029}$
u_0	$0.017^{+0.002}_{-0.002}$	$0.016^{+0.002}_{-0.001}$	$t_{0,S2}$	$7872.797^{+0.012}_{-0.024}$
t_E (days)	$33.380^{+2.966}_{-4.002}$	$35.513^{+3.026}_{-4.445}$	t_E	$34.435^{+3.215}_{-4.044}$
s	$0.529^{+0.012}_{-0.048}$	$1.964^{+0.210}_{-0.069}$	$u_{0,S1}$	$0.011^{+0.002}_{-0.002}$
q	$0.012^{+0.004}_{-0.002}$	$0.011^{+0.004}_{-0.002}$	$u_{0,S2}$	$0.015^{+0.002}_{-0.001}$
α	$2.723^{+0.006}_{-0.011}$	$2.725^{+0.006}_{-0.011}$	q_{flux}	$4.099^{+0.844}_{-0.489}$
ρ_*	≤ 0.010	≤ 0.009	ρ_*	...
$F_{S,\text{KMTC}}$	$0.014^{+0.002}_{-0.001}$	$0.013^{+0.002}_{-0.001}$	$F_{S,\text{KMTC}}$	$0.014^{+0.002}_{-0.001}$
$F_{B,\text{KMTC}}$	$0.327^{+0.001}_{-0.002}$	$0.328^{+0.001}_{-0.002}$	$F_{B,\text{KMTC}}$	$0.327^{+0.001}_{-0.002}$
$F_{S,\text{KMTS}}$	$0.013^{+0.002}_{-0.001}$	$0.012^{+0.002}_{-0.001}$	$F_{S,\text{KMTC}}$	$0.013^{+0.002}_{-0.001}$
$F_{B,\text{KMTS}}$	$0.329^{+0.001}_{-0.002}$	$0.330^{+0.001}_{-0.002}$	$F_{B,\text{KMTC}}$	$0.329^{+0.001}_{-0.002}$
$F_{S,\text{KMTA}}$	$0.011^{+0.002}_{-0.001}$	$0.010^{+0.002}_{-0.001}$	$F_{S,\text{KMTC}}$	$0.010^{+0.001}_{-0.001}$
$F_{B,\text{KMTA}}$	$0.312^{+0.001}_{-0.002}$	$0.313^{+0.001}_{-0.002}$	$F_{B,\text{KMTC}}$	$0.313^{+0.001}_{-0.001}$
<hr/>				
KMT-2017-BLG-1119				
χ^2/N_{data}	1495.733/1496	1502.058/1496	χ^2/N_{data}	1515.717/1496
t_0 (HJD')	$7969.862^{+0.009}_{-0.008}$	$7969.732^{+0.004}_{-0.004}$	$t_{0,S1}$	$7968.411^{+0.047}_{-0.025}$
u_0	$0.024^{+0.004}_{-0.003}$	$0.041^{+0.003}_{-0.002}$	$t_{0,S2}$	$7969.767^{+0.004}_{-0.003}$
t_E (days)	$3.536^{+0.375}_{-0.375}$	$3.561^{+0.146}_{-0.370}$	t_E	$2.588^{+0.153}_{-0.153}$
s	$0.872^{+0.009}_{-0.013}$	$1.140^{+0.028}_{-0.015}$	$u_{0,S1}$	$0.092^{+0.035}_{-0.017}$
q	$0.060^{+0.013}_{-0.014}$	$0.006^{+0.001}_{-0.001}$	$u_{0,S2}$	$0.050^{+0.005}_{-0.004}$
α	$0.699^{+0.045}_{-0.069}$	$3.061^{+0.009}_{-0.014}$	q_{flux}	$5.805^{+0.569}_{-1.039}$
ρ_*	$0.047^{+0.005}_{-0.007}$	$0.025^{+0.007}_{-0.001}$	ρ_*	...
$F_{S,\text{KMTC}}$	$0.151^{+0.017}_{-0.014}$	$0.139^{+0.023}_{-0.010}$	$F_{S,\text{KMTC}}$	$0.230^{+0.030}_{-0.020}$
$F_{B,\text{KMTC}}$	$0.244^{+0.014}_{-0.018}$	$0.257^{+0.009}_{-0.024}$	$F_{B,\text{KMTC}}$	$0.166^{+0.019}_{-0.011}$
$F_{S,\text{KMTS}}$	$0.102^{+0.008}_{-0.008}$	$0.100^{+0.007}_{-0.007}$	$F_{S,\text{KMTC}}$	$0.175^{+0.036}_{-0.022}$
$F_{B,\text{KMTS}}$	$0.311^{+0.008}_{-0.012}$	$0.313^{+0.006}_{-0.023}$	$F_{B,\text{KMTC}}$	$0.238^{+0.020}_{-0.037}$
$F_{S,\text{KMTA}}$	$0.107^{+0.012}_{-0.011}$	$0.107^{+0.022}_{-0.006}$	$F_{S,\text{KMTC}}$	$0.190^{+0.029}_{-0.019}$
$F_{B,\text{KMTA}}$	$0.289^{+0.010}_{-0.018}$	$0.289^{+0.006}_{-0.022}$	$F_{B,\text{KMTC}}$	$0.206^{+0.019}_{-0.030}$

NOTE. — For KMT-2017-BLG-0962, we present upper limits (3σ) of the ρ_* parameters for the 2L1S models. Because this event does not have caustic-crossings, the ρ_* parameters are not accurately measured (see Figure 6). For the 1L2S models of both events, the finite source effect is not considered for modeling.

of the close and wide cases) and 1L2S model are completely degenerate. The χ^2 differences between 1L2S and 2L1S are only ~ 0.6 and ~ 0.3 for the close and wide cases, respectively. Thus, we cannot claim a certain planet discovery.

3.4. Degeneracy in KMT-2017-BLG-1119

For KMT-2017-BLG-1119, we find that the observed light curve is also well-described by both interpretations. In Figure 2, we present light curves of these degenerate models with their geometries and residuals. In Table 1, we present the parameters of these degenerate models. We note that, in contrast to the close/wide degeneracy of the previous case, the degenerate solutions of the 2L1S interpretations of this event are not caused by the intrinsic symmetry in the lens equation. Indeed, these two degenerate solutions are caused by non-optimal coverage of the observations. These solutions are accidentally located in the close and wide region in the $s-q$ parameter space, respectively. We simply refer these local solutions as “close” and “wide” in this work.

In contrast to the previous case, these models show slight variations. The best-fit model, 2L1S (close), shows a low mass ratio ($q \sim 0.06$) with very short Einstein timescale ($t_E \sim 3.5$ days). This indicates that this event can be caused by a planetary lens system. However, this event also can be well described by the 1L2S interpretation, which implies that the planet would not exist. Quantitatively, the χ^2 differences between 1L2S and 2L1S (close and wide cases) are $\Delta\chi^2 \sim 20.0$

and 13.7 from the close and wide cases, respectively.

3.5. Higher-order Effects of the Interpretations

Even though both events have the 2L1S/1L2S degeneracy, it is possible that these events were caused by planetary lens systems. Thus, for the 2L1S interpretation, we check the possibility of measuring the annual microlens parallax (APRX: Gould 1992) because the microlens parallax is a key observable for directly determining the properties of the lens system. APRX is caused by the orbital motion of Earth. Thus, the Einstein timescale (t_E) is a direct indicator for estimating the possibility of detecting the APRX signal. Empirically, to detect the APRX signal, the event should last more than ~ 20 days. For KMT-2017-BLG-0962, t_E is about 33 days, which implies that there is a chance to detect the APRX signal in the light curve. Thus, we try to measure the APRX by introducing two additional parameters, $\pi_{E,N}$ and $\pi_{E,E}$, which indicate the north and east directions of the microlens parallax vector (π_E), respectively. From the model considering the APRX, we find χ^2 improvements, 13.0 and 0.1, for the close and wide cases, respectively. However, these improvements originate in fits of systematics in the baseline, which are caused by accidental caustic-crossing and approach (See Figure 3). This fact implies that the APRX is not significantly constrained in these fits. Thus, we cannot extract any useful information from the APRX model for this event. For KMT-2017-BLG-1119, t_E is only 3.5 days, which means that it is unlikely to exist the

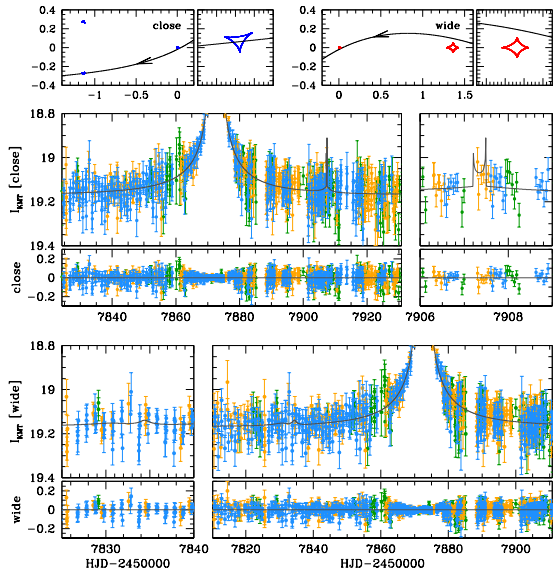


FIG. 3.— APRX models (2L1S) of KMT-2017-BLG-0962. Upper panels show geometries of the APRX models for the close (left) and wide (right) cases with zoom-ins where caustic-crossing and approach. Middle panels show the APRX model light curve (solid line) of the close case with a zoom-in where the part of caustic-crossing (left panels). Bottom panels show the APRX model light curve of the wide case. The zoom-in (right) shows the light curve part where the caustic approach. Bottom panels of each light curve show residuals between models and observations. The color scheme of the observations is identical to Figure 1.

APRX signal can be detected in the light curve. However, for the consistency, we also test the APRX model for this event. From the model, as expected, the APRX signal is not detected.

For the 1L2S interpretation, the binary sources orbit each other and conserve their angular momentum. This source-orbital motion can affect the light curve. In addition, the source-orbital effect can be a clue to resolving the 2L1S/1L2S degeneracy. Thus, we test the effect of the source-orbital motion by adopting the B-type parameterization with two additional orbital parameters (see Appendix for details of this parameterization). For KMT-2017-BLG-1119, there is no χ^2 improvement. This is expected considering the very short t_E of this event. In contrast, for KMT-2017-BLG-0962, we find a small χ^2 improvement ($\Delta\chi^2 \sim 8.7$) when the source-orbital effect is considered. We investigate this improvement using the cumulative χ^2 difference plot. See Figure 4. From the investigation, we find that the improvement mostly comes from the fitting of the “bump-like” feature in the baseline (HJD' ~ 8000). It is unclear whether this feature is real or due to some systematics in the baseline of the event. With $\Delta\chi^2 \sim 8.7$ for 2 additional degree of freedom, the significance is too low to claim a detection.

4. RESOLVING THE DEGENERACY

We now consider whether the 2L1S/1L2S degeneracy can be resolved in either of the two events. There are several methods that may be employed to resolve this degeneracy, most of which were discussed by Gaudi (1998). The first method is the detailed analysis of the light curve to check for small differences between the two models.

For KMT-2017-BLG-0962, the χ^2 difference between the 2L1S and 1L2S models is insignificant, and Figure 1 shows that the three models are quite similar. In contrast to the Gaudi (1998) case, there are no caustic-crossings. There exists only a smooth deviation from a 1L1S event. Thus, for this event,

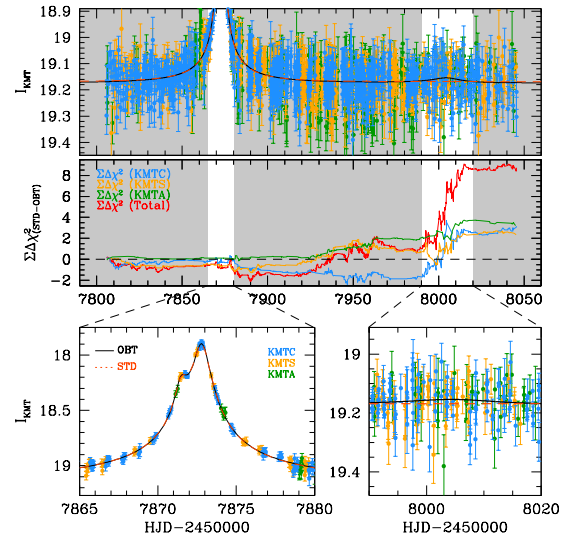


FIG. 4.— Cumulative χ^2 difference ($\Sigma\Delta\chi^2$) between static and source-orbital models (1L2S) of KMT-2017-BLG-0962. The upper panel shows the whole baseline observations with static (dashed line in scarlet) and source-orbital (solid line in black) model light curves. The bottom panel presents the $\Sigma\Delta\chi^2$ of each data set. The boxes in white show light curve zoom-ins for anomaly part (left) and the perturbation induced by the source-orbital motion effect (right).

the differences in the light curve are not sufficient to resolve the degeneracy.

For KMT-2017-BLG-1119, the best 2L1S model is preferred by $\Delta\chi^2 \sim 20$ over the 1L2S model. However, even though the degeneracy is formally broken, the distinction is not as strong as it appears. In Figure 5, we present plots of the cumulative χ^2 difference of each data set to investigate the origin of the χ^2 improvement. We find that the χ^2 difference comes from the KMTA and KMTC data sets. The KMTA observations contribute $\Delta\chi^2 \sim 6$ from HJD' ~ 7968 (see three middle panels of zoom-in in Figure 5). However, the KMTA data show systematic residuals to the 2L1S model, suggesting that a significant portion of the improvement could just be from fitting systematics in the data. This leaves a χ^2 improvement of just 14 from KMTC data. While this still indicates a preference for the 2L1S model, the physical parameters derived from the Bayesian analysis in Section 4.2 predict an extreme system in which the host itself is a massive planet. Thus, we should consider other means of testing the models to independently resolve the degeneracy.

The second method is to use the source-color information. Because the magnification of the 1L2S model is a weighted mean using the flux ratio of the sources (see Appendix A), the final magnification is wavelength dependent. Thus, if the binary sources have different colors (and the event really is a 1L2S event), we can measure the color change or difference during the perturbation from multi-band observations. However, unfortunately, the signal-to-noise ratio of V-band observations (the KMTNet regularly takes V-band images) for both events is too low to apply this method. Thus, we cannot resolve the degeneracy using this method.

Gaudi (1998) also proposed additional observations to resolve the degeneracy if the previous methods fail. One spectroscopic method requires taking spectra of the source both during and after the perturbations of the event. However, this method cannot be used after the events have ended. The other method requires photometrically and spectroscopically

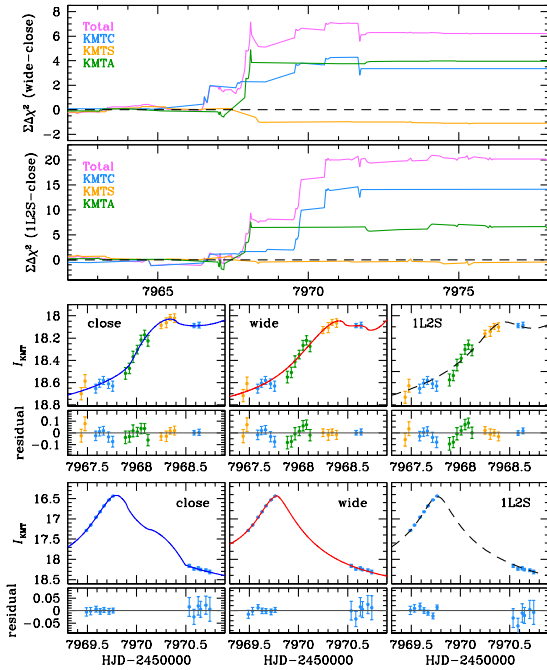


FIG. 5.— Cumulative χ^2 differences ($\Sigma\Delta\chi^2$) of degenerate models with zoom-ins for anomaly part of KMT-2017-BLG-1119. Upper two panels show the $\Sigma\Delta\chi^2$ of each data set and total $\Sigma\Delta\chi^2$. Lower six panels present zooms of anomaly parts with residuals of each model case.

monitoring of the source after the event to search for other signals induced by the binary source such as radial velocity variations due to orbital motion or eclipses. Given the faintness of the source(s), spectroscopic monitoring would be challenging. And given the source separations ($0.04\theta_E$ and $0.5\theta_E$ for KMT-2017-BLG-0962 and KMT-2017-BLG-1119, respectively), the probability of eclipses is extremely low.

In addition, Calchi Novati et al. (2018) presented a new method to resolve the 2L1S/1L2S degeneracy using simultaneous ground- and space-based observations. However, unfortunately, space-based data do not exist for these events (see footnote 2).

Thus, we consider another possibility to resolve the degeneracy using high-resolution follow-up observations to directly measure the magnitude of the source(s) for these events. For KMT-2017-BLG-1119, we found different source fluxes (F_S) for the 2L1S and 1L2S interpretations (see Table 1). If this event was caused by the planetary system, the magnitude of the source will be $I = 20.08 \pm 0.11$ and the lens is predicted to be dark. If this event was caused by binary sources, the integrated magnitude of the sources will be observed $I = 19.62 \pm 0.12$. We note that these expected I magnitudes are calibrated to the OGLE-III magnitude system by cross-matching between KMTNet and OGLE-III catalogs.

We check the expected brightness of the baseline object using observations taken from the Canada-France-Hawaii Telescope (CFHT) located at the Maunakea Observatories in 2018. From the stacked deep CFHT image (seeing $\sim 0.7''$), we can measure the brightness of the baseline object: $I_{\text{base}} = 19.62 \pm 0.05$ (we note that the CFHT instrumental magnitude is also calibrated to the OGLE-III magnitude system). This constraint strongly supports the conclusion that this event is caused by the 1L2S system. However, we cannot guarantee that the CFHT measurement completely excludes blend light from unrelated stars. Thus, the possibility of the 2L1S origin

cannot be clearly ruled out although it is strongly disfavored.

Thus, we consider an alternative constraint obtained from the Bayesian analysis (see Section 5.2). The 2L1S solution predicts a very low lens-source relative proper motion ($1-3 \text{ mas yr}^{-1}$). Thus, if observations were made a decade after the event and the source and lens were resolved, that would further confirm the 1L2S solution for which we expect both a stellar (luminous) lens and a “normal” relative proper motion ($3-5 \text{ mas yr}^{-1}$). Even if only the source proper motion were measured, if it were large ($\gtrsim 3 \text{ mas yr}^{-1}$), that would be a strong statistical argument in favor of the 1L2S solution.

In contrast, for KMT-2017-BLG-0962, we obtained almost identical values of the F_S , and the predicted lens-source relative proper motion is quite typical. Thus, for this event, high-resolution follow-up observations would not be helpful for resolving the degeneracy.

5. PROPERTIES OF PLANET CANDIDATES

5.1. Bayesian Analyses

Because we cannot measure the microlens parallax, we estimate the properties of these planet candidates using the Bayesian analyses. We build a prior by generating artificial microlensing events (the total number of simulated events is 4×10^7). To generate these events, we adopt the Galactic models from various studies: initial and present-day mass functions of Chabrier (2003), velocity distributions of Han & Gould (1995), and matter density profiles of the Galactic bulge and disk of Han & Gould (2003). When these artificial microlensing events are generated, the line of sight to the actual event is considered. This prior contains various information about host properties according to the event rate. Based on the event rate, we calculate the posterior probability distributions of the lens properties, by applying constraints obtained from the actual event.

The constraints are built in the form of weight functions, which are obtained from the t_E and ρ_* distributions of the actual event. In Figures 6 and 7, we present the distributions of selected parameters (t_E , ρ_* , and q), the first two of which are used to build the weight functions and determine the lens properties for KMT-2017-BLG-0962 and KMT-2017-BLG-1119, respectively. The distributions show a skewed Gaussian form, which we parameterize by,

$$W(x) = \eta e^{-\frac{1}{2}(\frac{x-\mu}{\sigma})^2} \left\{ 1 + \text{erf} \left[\frac{\alpha(x-\mu)}{\sqrt{2}\sigma} \right] \right\}, \quad (1)$$

where the function $\text{erf}[z] = (1/\sqrt{\pi}) \int_{-z}^z e^{-t^2} dt$. The variable x is t_E or ρ_* . The set of $(\eta, \mu, \sigma, \alpha)$ are fitting parameters. We use the MCMC algorithm to fit these parameters. The fitting results, i.e., t_E and ρ_* weight functions, $W(t_E)$ and $W(\rho_*)$, are presented in Figures 6 and 7 (cyan lines). In Table 2, we present the best-fit parameter sets of $W(t_E)$ and $W(\rho_*)$ for both events. The final weight function is $W = W(t_E)W(\rho_*)$. By applying the final weight function to the event rate, we construct probability distributions of the host mass (M_L), the distance to the lens (D_L), the physical Einstein ring radius (r_E), and the proper motion (μ). From these probability distributions, we can determine the properties of the planet candidate of each event.

We note that, for applying the $W(\rho_*)$ to the event rate, the angular source radius (θ_*) is required to convert from θ_E (for the artificial lensing events) to ρ_* ($\rho_* = \theta_*/\theta_E$). However, unfortunately, we do not have reliable V -band data to estimate

TABLE 2
THE BEST-FIT PARAMETERS OF WEIGHT FUNCTIONS

event model parameter	KMT-2017-BLG-0962				KMT-2017-BLG-1119			
	close	wide	close	wide	close	wide	close	wide
	$W(t_E)$	$W(\rho_*)$	$W(t_E)$	$W(\rho_*)$	$W(t_E)$	$W(\rho_*)$	$W(t_E)$	$W(\rho_*)$
η	0.706	0.593	0.672	0.597	0.762	0.853	0.661	0.912
μ	29.780	0.007	31.103	0.006	3.317	0.050	3.203	0.030
σ	4.745	0.004	5.452	0.004	0.322	0.007	0.372	0.005
α	1.683	-3.077	2.022	-3.164	1.367	-0.815	2.067	-0.571

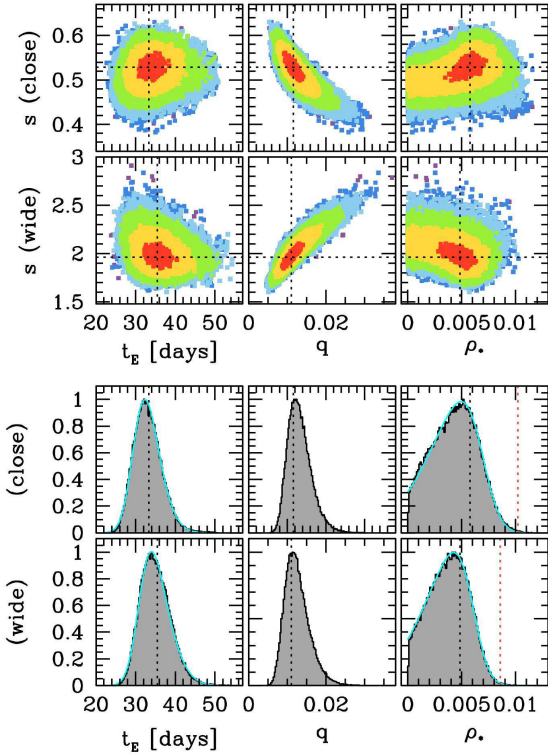


FIG. 6.— Distributions of t_E , q , and ρ_* parameters for KMT-2017-BLG-0962. The upper six panels present 2D distributions for the close and wide cases of the 2L1S model obtained from the MCMC chains. Each color represents $\Delta\chi^2$ between realization on the chain and the best-fit model: 1^2 (red), 2^2 (yellow), 3^2 (green), 4^2 (sky blue), 5^2 (blue), and 6^2 (purple). The lower six panels present 1D distributions of t_E , q , and ρ_* parameters for the close and wide cases. The cyan lines indicate weight functions constructed by the fitting of the skewed Gaussian function. The black dotted line indicates the parameter value of the best-fit model. The red dotted line in the ρ_* distributions represent the 3σ values.

θ_* using the conventional method of Yoo et al. (2004). Thus, we estimate the θ_* by adopting various studies. The apparent I magnitude of the source is determined from the F_S model parameter. Then, we estimate the intrinsic I magnitude of the source using mean extinction (adopted from Nishiyama et al. 2009 and Gonzalez et al. 2012) and the distance to the source (estimated using a relation of Nataf et al. 2013). For KMT-2017-BLG-0962, $A_I \sim 3.9$, and for KMT-2017-BLG-1119, $A_I \sim 1.7$, so $I_0 \sim 18.8$ and ~ 18.3 , respectively. From this magnitude, the intrinsic color of the source is estimated by adopting properties of dwarfs (Pecaut et al. 2012; Pecaut & Mamajek 2013). Lastly, θ_* is estimated using the color/surface-brightness relation adopted from Kervella et al. (2004). As a result, the estimated θ_* we used are ~ 0.58 and $\sim 0.60 \mu\text{as}$ for KMT-2017-BLG-0962 and KMT-2017-BLG-1119, respectively.

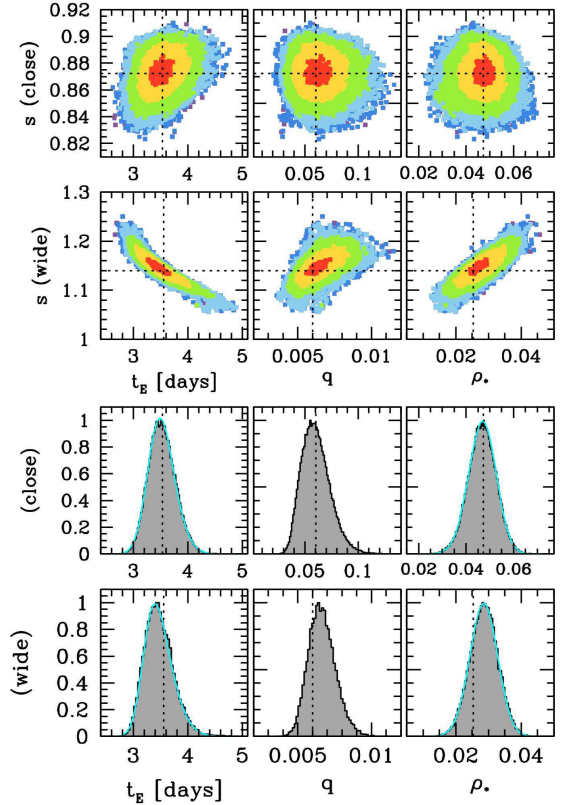


FIG. 7.— Distributions of t_E , q , and ρ_* parameters for KMT-2017-BLG-1119. The description is the same as for Figure 6.

5.2. Bayesian Results

For KMT-2017-BLG-0962, in Figure 8, we present the probability distributions of the lens properties for the close and wide solutions. Because we cannot rule out the possibility of stellar remnant hosts, the distributions are constructed using Galactic priors with and without stellar remnants as hosts of the lens system. In Table 3, we present median values of the distributions as representative of the lens system with 68% (1σ) confidence intervals. The Bayesian results indicate that this event can be produced by a planetary system consisting of a mid-M dwarf host star and a super Jupiter-mass planet orbiting beyond the snow line.

For KMT-2017-BLG-1119, the 2L1S interpretation is strongly disfavored considering both the CFHT measurement of the baseline object and the statistical argument of the proper motion. Although the 2L1S solution is disfavored, we report the Bayesian results for completeness. In Figure 9, we also present the probability distributions similar to the previous event. Because the timescale of this event is particularly short, the distributions with and without stellar remnant hosts show identical results. Thus, we present one case. In Table 3,

TABLE 3
PROPERTIES OF PLANETARY SYSTEM CANDIDATES

event model	KMT-2017-BLG-0962 close	KMT-2017-BLG-0962 wide	KMT-2017-BLG-1119 close	KMT-2017-BLG-1119 wide
w/ stellar remnants				
$M_{\text{host}} (M_{\odot})$	$0.46_{-0.29}^{+0.34}$	$0.48_{-0.30}^{+0.34}$	$0.010_{-0.007}^{+0.031}$	$0.013_{-0.009}^{+0.035}$
$M_{\text{planet}} (M_{\text{J}})$	$5.6_{-3.7}^{+4.7}$	$5.6_{-3.6}^{+4.5}$	$0.61_{-0.45}^{+1.95}$	$0.08_{-0.06}^{+0.22}$
$D_{\text{L}} (\text{kpc})$	$6.4_{-1.3}^{+1.3}$	$6.4_{-1.8}^{+1.3}$	$8.8_{-1.1}^{+1.0}$	$8.5_{-1.0}^{+1.1}$
$a_{\perp} (\text{au})$	$1.2_{-0.5}^{+0.5}$	$4.7_{-1.8}^{+1.9}$	$0.11_{-0.02}^{+0.02}$	$0.24_{-0.04}^{+0.06}$
$a_{\text{snow}} (\text{au})$	$1.2_{-0.8}^{+0.9}$	$1.3_{-0.8}^{+0.9}$	$0.03_{-0.02}^{+0.08}$	$0.03_{-0.02}^{+0.10}$
$\mu (\text{mas yr}^{-1})$	$4.3_{-1.9}^{+2.4}$	$4.2_{-1.9}^{+2.4}$	$1.5_{-0.2}^{+0.3}$	$2.6_{-0.4}^{+0.6}$
w/o stellar remnants				
$M_{\text{host}} (M_{\odot})$	$0.38_{-0.24}^{+0.40}$	$0.40_{-0.25}^{+0.41}$		
$M_{\text{planet}} (M_{\text{J}})$	$4.7_{-3.0}^{+5.2}$	$4.7_{-3.9}^{+5.1}$		
$D_{\text{L}} (\text{kpc})$	$6.4_{-1.9}^{+1.3}$	$6.3_{-1.9}^{+1.3}$		
$a_{\perp} (\text{au})$	$1.1_{-0.5}^{+0.5}$	$4.3_{-1.7}^{+2.0}$		
$a_{\text{snow}} (\text{au})$	$1.0_{-0.6}^{+1.1}$	$1.1_{-0.7}^{+1.1}$		
$\mu (\text{mas yr}^{-1})$	$4.1_{-1.9}^{+2.5}$	$4.1_{-1.8}^{+2.4}$		

NOTE. — For KMT-2017-BLG-1119, the median values with and without stellar remnant hosts are identical. Thus, we present one case to avoid clutter.

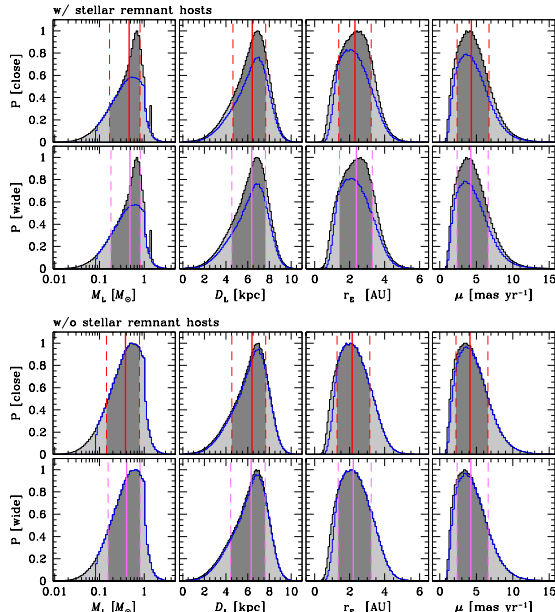


FIG. 8.— Probability distributions of the lens properties for KMT-2017-BLG-0962. The upper six panels show the probability distributions of the host mass (M_{L}), the distance to the lens (D_{L}), the physical Einstein ring radius (r_{E}), and the relative lens-source proper motion (μ) for the close and wide cases. These distributions are constructed from the Galactic prior with stellar remnant hosts. The lower six panels show the probability distributions for the same lens properties, which are constructed from the Galactic prior without stellar remnant hosts. The solid and dashed vertical lines indicate the median value and 68% confidence interval (1σ uncertainty) of each property, respectively. The red and pink represent close and wide cases, respectively. The distributions in blue indicate the probability distributions considering only luminous hosts.

we also present median values of the distributions.

The Bayesian results suggest that the lens system of KMT-2017-BLG-1119 may be particularly interesting. For the close case, the lens system consists of a planet-like host ($\sim 0.010 M_{\odot}$) and a sub-Jovian planet ($\sim 0.6 M_{\text{Jupiter}}$). For the wide case, the lens system consists of a planet-like host ($\sim 0.013 M_{\odot}$) and a Neptune-class planet ($\sim 25 M_{\text{Earth}}$). For both cases, the hosts can be planets, which means that the planetary system might be a free-floating planetary system.

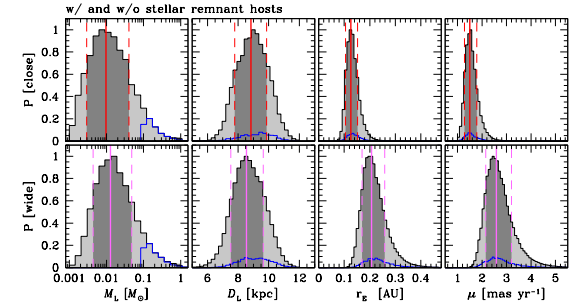


FIG. 9.— Probability distributions of the lens properties for KMT-2017-BLG-1119. The description is the same as for Figure 8. In this case, the probability distributions with and without stellar remnant hosts are identical. Thus, we present only one case to avoid clutter.

Such an exceptional result would require exceptional evidence, which does not exist. Thus, the unusual nature of the predicted lens system lends additional weight to the conclusion that the competing 1L2S solution is correct.

6. CONCLUSION

We have presented the analysis of two microlensing events with candidate planets. From Bayesian analysis, we determine the properties of the planet candidates. For KMT-2017-BLG-0962, the lens system may consist of a super Jupiter-mass planet and a mid-M dwarf host. However, the severe 2L1S/1L2S degeneracy of this event, which is unresolvable, prevents claiming this planet discovery with certainty. For KMT-2017-BLG-1119, the 2L1S interpretation would indicate that the lens system consists of a sub-Jupiter-mass planet and a planet-like host. However, the additional constraints strongly support the 1L2S interpretation rather than this potential interesting planetary system.

The 2L1S/1L2S degeneracies described in this work (and also the degeneracy in Jung et al. 2017a) are far different from the degeneracy for small, short-duration positive anomalies shown in Gaudi (1998). The anomalies are of much longer duration and affect a significant fraction of the light curves, yet the degeneracy remains. In addition, the magnitude difference (ΔI) between the two sources is not very extreme ($\Delta I < 2.0$) in contrast to Gaudi’s case. These events are similar to the event recently analyzed in Dominik et al. (2019).

These cases show that the 2L1S/1L2S degeneracy can exist for a wide range of planetary events and for much less extreme binary source systems. Because binary stars are common and this degeneracy has proven not to be limited to a rare subset of binaries, the 2L1S/1L2S degeneracy may be a bigger problem for the discovery of planets than previously thought.

This research has made use of the KMTNet system operated by the Korea Astronomy and Space Science Institute (KASI) and the data were obtained at three host sites of CTIO in Chile, SAAO in South Africa, and SSO in Australia. Work by IGS and AG was supported by JPL grant 1500811. AG ac-

knowledges the support from NSF grant AST-1516842. AG received support from the European Research Council under the European Unions Seventh Framework Programme (FP 7) ERC Grant Agreement n. [321035]. Work by CH was supported by the grant (2017R1A4A1015178) of National Research Foundation of Korea. This research uses data obtained through the Telescope Access Program (TAP), which has been funded by the National Astronomical Observatories, Chinese Academy of Sciences, and the Special Fund for Astronomy from the Ministry of Finance. Work by MTP was partially supported by NASA grants NNX16AC62G and NNG16PJ32C. Work by WZ and PF was supported by CanadaFranceHawaii Telescope (CFHT).

APPENDIX

TWO PARAMETERIZATIONS OF THE 1L2S INTERPRETATION

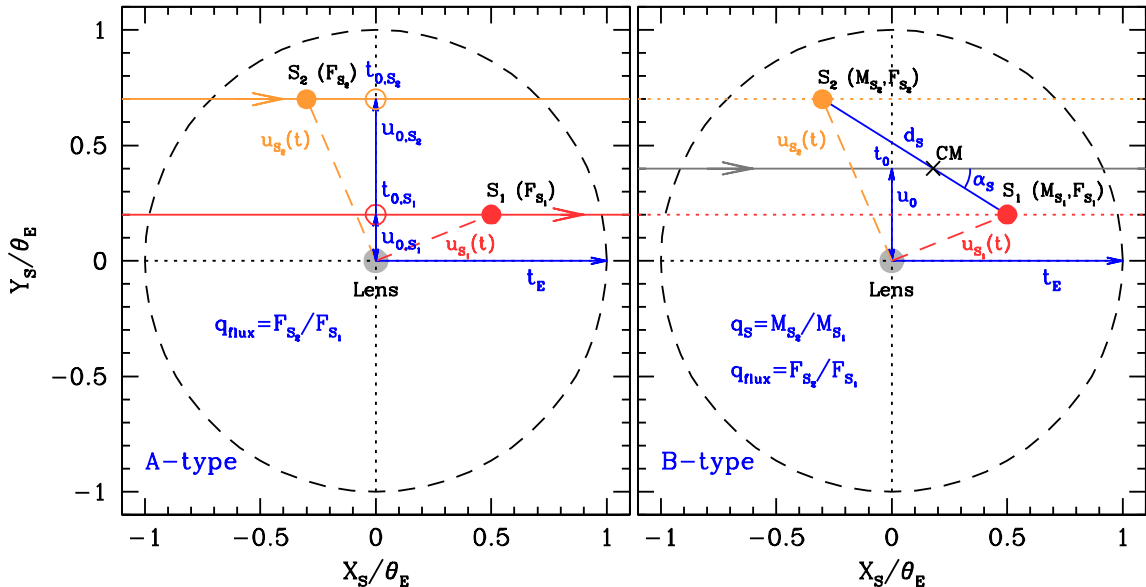


FIG. 10.— Conceptual geometries of the 1L2S interpretation. The left and right panels present the geometries of the A-type and B-type parameterizations, respectively. The blue text indicates parameters. The index $i = 1$ and 2 indicate the first source (S_1) and second source (S_2), respectively. The F_{S_i} and M_{S_i} denote the flux and mass of each source. “CM” denotes the barycenter (i.e., center of mass) of the binary-source system.

In Figure 10, we present conceptual geometries of the 1L2S interpretation for two types of parameterizations. The A-type parameterization (see the left panel of Figure 10) requires six parameters ($t_{0,S1}$, $t_{0,S2}$, $u_{0,S1}$, $u_{0,S2}$, t_E , and q_{flux}). The first five parameters are directly related to the source trajectories: $t_{0,S1}$ and $t_{0,S2}$ are the time when each source most closely approaches the reference position (i.e., the position of the lens), $u_{0,S1}$ and $u_{0,S2}$ represent the closest separation between each source and the reference position at the time of $t_{0,S1}$ and $t_{0,S2}$, respectively, t_E is the Einstein timescale. We use one t_E parameter assuming that the relative lens-source speeds are same for both sources, i.e., a comoving binary-source system. The last parameter, $q_{\text{flux}} = F_{S2}/F_{S1}$ is the flux ratio of the sources. The role of q_{flux} is to weight the two 1L1S light curves produced by the individual sources.

By adopting this parameterization, the position of each source as a function of time (t) is defined in Cartesian coordinates normalized by θ_E as

$$[X_{S_i}(t), Y_{S_i}(t)] = \left[\left(\frac{t - t_{0,S_i}}{t_E} \right), u_{0,S_i} \right] ; i = 1, 2. \quad (\text{A1})$$

According to the positions of the sources, the magnification of each source, $A_{S_i}(t)$, is defined as

$$A_{S_i}(t) = \frac{u_{S_i}^2(t) + 2}{u_{S_i}(t) \sqrt{u_{S_i}^2(t) + 4}} ; u_{S_i}(t) = [X_{S_i}^2(t) + Y_{S_i}^2(t)]^{\frac{1}{2}} ; i = 1, 2. \quad (\text{A2})$$

These magnifications are superposed by weighting by the ratio of source fluxes, $q_{\text{flux}} = F_{S2}/F_{S1}$. Then, the final magnification of the lensing light curve, $A(t)$, is calculated as

$$A(t) = \frac{A_{S1}(t) + q_{\text{flux}} A_{S2}(t)}{1 + q_{\text{flux}}}. \quad (\text{A3})$$

This model light curve in the magnification scale is converted to the flux scale of each data set for comparison to the observations using two additional parameters, F_S and F_B (similar to those of the 2L1S interpretation). These additional parameters are determined using the least-square fitting method.

The merit of this A-type parameterization is that it is possible to directly guess the initial values of most parameters (except q_{flux}) from the observed light curve. However, the A-type parameterization has a disadvantage that it is difficult to apply higher-order effects, especially the orbital motion of the binary-source system.

Thus, we introduce an alternative parameterization, B-type (see right panel of Figure 10), which considers the motion of the barycenter of the binary-source system, rather than the motion of each source. To describe the barycenter motion, it requires three parameters (t_0 , u_0 , t_E): t_0 is the time when the barycenter closely approaches to the reference position, u_0 is the closest separation at the time of t_0 , and t_E is the Einstein timescale. To derive the trajectory of each source from the barycenter trajectory, three additional parameters (d_S , q_S , α_S) are required to describe the binary-source system: d_S is the projected separation between the sources, $q_S = M_{S_2}/M_{S_1}$ is a mass ratio of the source stars, and α_S is an angle between the axis of the binary-source and the barycenter trajectory. In addition, there is the last parameter (q_{flux}) that is identical to that of the A-type parameterization.

By adopting this parameterization, the source positions are defined as

$$\begin{bmatrix} X_{S_i}(t) \\ Y_{S_i}(t) \end{bmatrix} = \begin{bmatrix} X_{\text{CM}}(t) \pm r_{S_i} \cos \alpha_S \\ Y_{\text{CM}}(t) \mp r_{S_i} \sin \alpha_S \end{bmatrix} ; [X_{\text{CM}}(t), Y_{\text{CM}}(t)] = \left[\left(\frac{t-t_0}{t_E} \right), u_0 \right] ; i = 1, 2 , \quad (\text{A4})$$

where the r_{S_1} and r_{S_2} are the separations between the barycenter and each source, which are defined as

$$r_{S_1} = d_S \left(\frac{q_S}{1+q_S} \right) ; r_{S_2} = d_S \left(\frac{1}{1+q_S} \right) . \quad (\text{A5})$$

Based on the positions of the source, the final model light curve is constructed in the same way as the previous parameterization (see Equations A2 and A3).

This B-type parameterization has merit when higher-order effects are considered. In particular, the orbital motion of the binary-source can be easily introduced because the binary source positions are defined from the barycenter. To introduce the source-orbital motion, two additional parameters, dd_S/dt and $d\alpha_S/dt$, are required. These parameters are the variation rates of d_S and α_S to describe a partial orbit of the binary-source system. The variations are derived as

$$d'_S = d_S + \frac{dd_S}{dt} (t - t_{\text{ref}}) ; \alpha'_S = \alpha_S + \frac{d\alpha_S}{dt} (t - t_{\text{ref}}) , \quad (\text{A6})$$

where t_{ref} is a reference time for describing the orbital motion of sources (we set $t_{\text{ref}} = t_0$ for the modeling in this work). Thus, the source trajectories are varied by the source-orbital motion, which are described by modifying Equations A4 and A5 as,

$$\begin{bmatrix} X'_{S_i}(t) \\ Y'_{S_i}(t) \end{bmatrix} = \begin{bmatrix} X_{\text{CM}}(t) \pm r'_{S_i} \cos \alpha'_S \\ Y_{\text{CM}}(t) \mp r'_{S_i} \sin \alpha'_S \end{bmatrix} \text{ where } r'_{S_1} = d'_S \left(\frac{q_S}{1+q_S} \right) ; r'_{S_2} = d'_S \left(\frac{1}{1+q_S} \right) . \quad (\text{A7})$$

However, the downside of this B-type parameterization is that it is particularly difficult to guess the initial parameters for describing the binary-source system (i.e., d_S , q_S , and α_S). Thus, usually, this parameterization is only adopted for testing higher-order effects.

REFERENCES

- Beaulieu, J.-P., Bennett, D. P., Fouqué, P., et al. 2006, *Nature*, 439, 437
 Calchi Novati, S., Skowron, J., Jung, Y. K., et al. 2018, *AJ*, 155, 261
 Chabrier, G. 2003, *PASP*, 115, 763
 Dominik, M. 1999, *å*, 349, 108
 Dominik, M., Bachelet, E., Bozza, V., et al. 2019, *MNRAS*, in press
 Dunkley, J., Bucher, M., Ferreira, P. G., et al. 2005, *MNRAS*, 356, 925
 Gaudi, B. S. 1998, *ApJ*, 506, 533
 Griest, K., & Safizadeh, N. 1998, *ApJ*, 500, 37
 Gonzalez, O. A., Rejkuba, M., Zoccali, M., et al. 2012, *A&A*, 543, A13
 Gould, A. 1992, *ApJ*, 392, 442
 Han, C., & Gould, A. 1995, *ApJ*, 447, 53
 Han, C., & Gould, A. 2003, *ApJ*, 592, 172
 Hwang, K.-H., Choi, J.-Y., Bond, I. A., et al. 2013, *ApJ*, 778, 55
 Hwang, K.-H., Udalski, A., Bond, I. A., et al. 2018, *AJ*, 155, 259
 Jung, Y. K., Udalski, A., Yee, J. C., et al. 2017a, *AJ*, 153, 129
 Jung, Y. K., Udalski, A., Bond, I. A., et al. 2017b, *ApJ*, 841, 75
 Kervella, P., Bersier, D., Mourard, D., et al. 2004, *A&A*, 428, 587
 Kim, S.-L., Lee, C.-U., Park, B.-G., et al. 2016, *JKAS*, 49, 37
 Kim, D.-J., Kim, H.-W., Hwang, K.-H., et al. 2018, *AJ*, 155, 76
 Nataf, D. M., Gould, A., Fouqué, P., et al. 2013, *ApJ*, 769, 88
 Nishiyama, S., Tamura, M., Hatano, H., et al. 2009, *ApJ*, 696, 1407
 Pecaut, M. J., Mamajek, E. E., & Bubar, E. J. 2012, *ApJ*, 746, 154
 Pecaut, M. J., & Mamajek, E. E. 2013, *ApJS*, 208, 9
 Yee, J. C., Gould, A., Beichman, C., et al. 2015, *ApJ*, 810, 155
 Yoo, J., DePoy, D. L., Gal-Yam, A., et al. 2004, *ApJ*, 603, 139